Global partitioning of NO_x sources using satellite observations: Relative roles of fossil fuel combustion, biomass burning and soil emissions

Lyatt Jaeglé,[a] Linda Steinberger,[a] Randall V. Martin[bc] and Kelly Chance[c]

[a] *Department of Atmospheric Sciences, University of Washington, Seattle, Washington, USA. E-mail: jaegle@atmos.washington.edu*
[b] *Department of Physics and Atmospheric Science, Dalhousie University, Halifax Canada*
[c] *Harvard-Smithsonian Center for Astrophysics, Cambridge, Massachusetts USA*

Received 10th February 2005, Accepted 22nd February 2005
First published as an Advance Article on the web 11th May 2005

We use space-based observations of NO_2 columns from the Global Ozone Monitoring Experiment (GOME) to derive monthly top-down NO_x emissions for 2000 *via* inverse modeling with the GEOS-CHEM chemical transport model. Top-down NO_x sources are partitioned among fuel combustion (fossil fuel and biofuel), biomass burning and soils by exploiting the spatio-temporal distribution of remotely sensed fires and *a priori* information on the location of regions dominated by fuel combustion. The top-down inventory is combined with an *a priori* inventory to obtain an optimized *a posteriori* estimate of the relative roles of NO_x sources. The resulting *a posteriori* fuel combustion inventory (25.6 TgN year^{-1}) agrees closely with the *a priori* (25.4 TgN year^{-1}), and errors are reduced by a factor of 2, from ±80% to ±40%. Regionally, the largest differences are found over Japan and South Africa, where *a posteriori* estimates are 25% larger than *a priori*. *A posteriori* fuel combustion emissions are aseasonal, with the exception of East Asia and Europe where winter emissions are 30–40% larger relative to summer emissions, consistent with increased energy use during winter for heating. Global *a posteriori* biomass burning emissions in 2000 resulted in 5.8 TgN (compared to 5.9 TgN year^{-1} in the *a priori*), with Africa accounting for half of this total. *A posteriori* biomass burning emissions over Southeast Asia/India are decreased by 46% relative to *a priori*; but over North equatorial Africa they are increased by 50%. *A posteriori* estimates of soil emissions (8.9 TgN year^{-1}) are 68% larger than *a priori* (5.3 TgN year^{-1}). The *a posteriori* inventory displays the largest soil emissions over tropical savanna/woodland ecosystems (Africa), as well as over agricultural regions in the western U.S. (Great Plains), southern Europe (Spain, Greece, Turkey), and Asia (North China Plain and North India), consistent with field measurements. Emissions over these regions are highest during summer at mid-latitudes and during the rainy season in the Tropics. We estimate that 2.5–4.5 TgN year^{-1} are emitted from N-fertilized soils, at the upper end of previous estimates. Soil and biomass burning emissions account for 22% and 14% of global surface NO_x emissions, respectively. We infer a significant role for soil NO_x emissions at northern mid-latitudes during summer, where they account for nearly half that of the fuel combustion source, a

doubling relative to the *a priori*. The contribution of soil emissions to background ozone is thus likely to be underestimated by the current generation of chemical transport models.

1. Introduction

Human activities have led to a three- to six-fold increase in nitrogen oxides ($NO_x = NO + NO_2$) emissions since pre-industrial times.[1] These large anthropogenic emissions, mostly resulting from fossil fuel combustion and biomass burning, are superimposed on natural sources of NO_x, which include microbial processes in soils, lightning and transport from the stratosphere.[2] While the contribution of fossil fuel combustion to the global NO_x budget is relatively well known (20–24 TgN year^{-1}), estimates of the other surface NO_x sources remain highly uncertain: biomass burning (3–13 TgN year^{-1}) and soil-atmosphere exchange (4–21 TgN year^{-1}).[3]

Improved estimates of NO_x emissions are crucial to better understanding regional and global ozone air pollution, acid deposition, and climate change. Current NO_x inventories are based on "bottom-up" estimates which aggregate information from diverse sources: country-by-country statistics on fuel and land use, agricultural data, estimates of burned areas, observations of NO_x emissions ratios in pollution plumes, and local measurements of soil fluxes.

Space-based observations of NO_2 columns from the Global Ozone Monitoring Experiment (GOME)[4,5] on board the European Remote Sensing (ERS-2) satellite can provide independent "top-down" constraints on global surface NO_x emissions.[6] Martin *et al.*[7] demonstrated how GOME tropospheric NO_2 columns can be related to surface NO_x emissions *via* inverse modeling, thus deriving a top-down emission inventory. When combined with a bottom-up inventory, these top-down emissions can reduce significantly the uncertainties in NO_x emissions.

In this study, we build on the work of Martin *et al.*,[7] and demonstrate how added information from satellite observations of fires and from the location of fossil fuel dominated regions can help to partition GOME top-down NO_x sources among fuel combustion (fossil fuel and biofuel), biomass burning, and soil emissions. This allows us to examine the magnitude, geographical distribution and seasonal variations of these individual sources and compare them to bottom-up estimates. We previously applied this method to examine NO_x sources over Africa.[8] Here, we improve on this method and apply it to the global NO_x budget for the year 2000.

In section 2 we describe the bottom-up NO_x emissions inventory used as the *a priori* in our analysis. In section 3, we infer top-down surface NO_x emissions from GOME NO_2 column observations, and describe a means for partitioning these emissions. The partitioned top-down and *a priori* inventories are combined into an optimized *a posteriori* inventory in section 4. We discuss our results in section 5, and compare our global *a posteriori* partitioning of surface NO_x sources to previous studies in section 6. Conclusions are given in section 7.

2. *A priori* NO_x emission inventory

We use NO_x emissions from the GEOS-CHEM global model of tropospheric chemistry[9] as our *a priori* global NO_x inventory. This inventory was previously described[7] and includes emissions from fossil fuel (23.3 TgN year^{-1}), biofuel[10] (2.2 TgN year^{-1}), biomass burning[11,12] (5.9 TgN year^{-1}), soils (5.3 TgN year^{-1}), aircraft (0.05 TgN year^{-1}), stratosphere-troposphere exchange (0.1 TgN year^{-1}), and lightning (3.5 TgN year^{-1}). More specifically, anthropogenic emissions are from the Global Emission Inventory Activity (GEIA),[13] scaled to 1998 as described in Bey *et al.*[9] The biomass burning inventory includes interannual and seasonal variability as derived by Duncan *et al.*,[12] using satellite observations of fires from the Along Track Scanning Radiometer (ATSR) and aerosols from the Total Ozone Monitoring Spectrometer (TOMS). The algorithm of Yienger and Levy[14] is applied to calculate soil emissions, with the canopy reduction factor described in Wang *et al.*[15] All emissions are on a 2° latitude by 2.5° longitude horizontal resolution. Tables 1–4 summarize the surface emission inventory for the individual regions shown in Fig. 1. In addition, the middle column of Fig. 2 illustrates the spatial distribution of these surface sources. Here and in the rest of the paper we combine fossil fuel and biofuel emissions into a single "fuel combustion" category.

Table 1 Annual surface NO_x emissions and relative errors for 2000[a]

	Total surface NO_x emissions/TgN year^{-1}			
	A priori	GOME	*A posteriori*	M2003[b]
(a) United States	6.8 (1.4)	8.3 (1.5)	7.4 (1.3)	7.3
(b) Europe	5.5 (1.7)	6.2 (1.5)	6.2 (1.4)	6.3
(c) East Asia	5.3 (2.0)	6.6 (1.5)	6.3 (1.5)	6.0
(d) Japan	0.54 (1.5)	0.81 (1.5)	0.67 (1.3)	0.73
(e) Mideast	1.1 (2.1)	1.6 (1.5)	1.3 (1.4)	1.2
(f) S. Africa	0.36 (3.5)	0.56 (1.6)	0.48 (1.5)	0.41
(g) SE Asia/India	4.9 (1.8)	2.4 (2.0)	4.3 (1.6)	3.9
(h) N. equatorial Africa	2.2 (2.3)	3.7 (1.6)	3.3 (1.5)	2.7
(i) S. equatorial Africa	2.4 (2.6)	2.6 (1.7)	2.5 (1.6)	2.3
(j) Central America	1.7 (2.0)	1.3 (1.9)	1.5 (1.6)	1.4
(k) S. America	2.7 (2.1)	2.3 (1.9)	2.8 (1.7)	2.4
(l) Australia	1.0 (2.3)	0.94 (2.2)	1.2 (1.8)	0.94
Global	36.5 (2.0)	39.7 (1.6)	40.3 (1.5)	37.8

[a] Surface NO_x emissions include fossil fuel combustion, biofuel combustion, biomass burning and soil emissions. Relative errors are indicated in parentheses. [b] *A posteriori* emissions inventory from Martin *et al.*[7] based on GOME 1996–1997 NO_2 columns.

Following Martin *et al.*,[7] we estimate the relative errors for the fuel combustion emissions as the ratio of *a priori* to EDGAR v3.2 1995 emissions.[16] For biomass burning and soils we use an estimate of the relative error of a factor of 3, reflecting the range of global estimates for both sources.[1] The overall *a priori* error is smaller than 1.5 ($\pm$50%) over regions dominated by fuel combustion emissions but increases to values above 2.5 ($\pm$150%) over the rest of the world (Table 1 and Fig. 2e). On local and monthly scales, the actual *a priori* errors for soil and biomass burning emissions might be higher than 3. However, because the top-down errors are generally smaller than a factor of 3 (section 3.4), our *a posteriori* will be dominated by the top-down constrains on soil and biomass burning emissions (see section 4), and thus a more detailed evaluation of *a priori* errors is not necessary for our analysis.

The *a priori* inventory is used to conduct a tropospheric O_3–NO_x–hydrocarbons simulation with the GEOS-CHEM model (version 5.05, http://www-as.harvard.edu/chemistry/trop/geos) for the year 2000. The model is driven by assimilated meteorological fields from the Goddard Earth Observing System (GEOS) Global Modeling and Assimilation Office, with a 2° latitude by

Table 2 Annual fuel combustion NO_x emissions for 2000

	Fuel combustion[a] emissions/TgN year^{-1}			
	A priori	GOME	*A posteriori*	EDGAR 3.2[16]
(a) United States	6.3 (1.4)	7.1 (1.5)	6.4 (1.2)	6.0
(b) Europe	4.9 (1.7)	4.6 (1.6)	4.9 (1.4)	6.7
(c) East Asia	4.8 (2.0)	5.3 (1.7)	5.2 (1.5)	4.7
(d) Japan	0.53 (1.6)	0.80 (1.5)	0.66 (1.3)	0.81
(e) Mideast	0.93 (2.1)	1.1 (1.6)	0.93 (1.4)	0.62
(f) S. Africa	0.27 (3.9)	0.39 (1.5)	0.33 (1.4)	0.38
(g) SE Asia/India	3.2 (1.6)	1.8 (2.0)	3.0 (1.4)	3.2
(h) N. equatorial Africa	0.40 (1.5)	0.39 (1.6)	0.39 (1.3)	0.44
(i) S. equatorial Africa	0.18 (1.8)	0.16 (1.9)	0.18 (1.5)	0.20
(j) Central America	1.0 (1.8)	0.78 (1.7)	0.89 (1.3)	0.85
(k) S. America	1.0 (1.5)	0.72 (1.8)	1.0 (1.4)	0.81
(l) Australia	0.31 (1.8)	0.19 (2.2)	0.31 (1.6)	0.38
Global	25.4 (1.8)	24.6 (1.6)	25.6 (1.4)	26.1

[a] Includes fossil fuel and biofuel emissions. Relative errors are indicated in parentheses.

Table 3 Annual biomass burning NO_x emissions for 2000

	Biomass burning emissions/TgN year^{-1}			
	A priori	GOME	*A posteriori*	GWEM 1.4[41]
(a) United States	0.11 (3)	0.17 (1.5)	0.12 (1.7)	0.05
(b) Europe	0.09 (3)	0.30 (1.5)	0.19 (1.7)	0.10
(c) East Asia	0.13 (3)	0.20 (1.5)	0.18 (1.7)	0.28
(d) Japan	0.00 (3)	0.00 (1.5)	0.00 (1.8)	0.01
(e) Mideast	0.00 (3)	0.03 (1.5)	0.02 (1.5)	0.00
(f) S. Africa	0.03 (3)	0.07 (1.5)	0.05 (1.8)	0.10
(g) SE Asia/India	1.1 (3)	0.28 (1.7)	0.61 (2.5)	0.16
(h) N. equatorial Africa	0.77 (3)	1.3 (1.5)	1.2 (1.5)	1.4
(i) S. equatorial Africa	1.8 (3)	1.8 (1.6)	1.7 (1.5)	1.4
(j) Central America	0.37 (3)	0.25 (1.8)	0.30 (2.0)	0.04
(k) S. America	0.87 (3)	0.81 (1.7)	0.81 (1.9)	0.16
(l) Australia	0.33 (3)	0.38 (1.8)	0.40 (1.9)	0.43
Global	5.9 (3)	5.7 (1.6)	5.8 (1.8)	5.0

2.5° longitude horizontal resolution and 30 vertical levels. The resulting NO_2 columns for four months (January, April, June and August 2000), chosen for illustrative purpose, are displayed on Fig. 3 (middle panels). These columns map onto surface NO_x emissions because of the short lifetime of NO_x (less than a day) and the large NO_2/NO_x ratio in the boundary layer.

3. Top-down NO_x emission inventory from GOME

3.1. The GOME instrument and retrieval

The GOME instrument is a nadir-viewing spectrometer, which detects absorption of atmospheric NO_2 in the visible by measuring backscattered solar radiation. Global coverage is achieved in 3 d with a ground footprint of 320 km × 40 km (cross track × along track). Slant columns of NO_2 are retrieved for the year 2000 by non-linear least-square fitting of backscattered radiance spectra.[17] Our conversion from slant columns to tropospheric NO_2 columns takes into account the influence of stratospheric columns and instrument biases, and includes scattering by the surface, clouds, aerosols, and gases.[7,18]

We only consider scenes where clouds contribute to less than 50% of backscattered radiation, corresponding to cloud or snow cover <40%. The monthly mean uncertainties for a 2° × 2.5° grid box in the retrieved GOME tropospheric NO_2 columns include a 30% relative error from the

Table 4 Annual soil NO_x emissions for 2000

	Soil emissions/TgN year^{-1}		
	A priori	GOME	*A posteriori*
(a) United States	0.41 (3)	1.0 (1.5)	0.86 (1.7)
(b) Europe	0.48 (3)	1.3 (1.5)	1.1 (1.7)
(c) East Asia	0.42 (3)	1.1 (1.6)	0.94 (1.7)
(d) Japan	0.01 (3)	0.0 (1.6)	0.01 (2.6)
(e) Mideast	0.17 (3)	0.53 (1.6)	0.40 (1.6)
(f) S. Africa	0.06 (3)	0.10 (2.0)	0.10 (2.0)
(g) SE Asia/India	0.59 (3)	0.32 (2.2)	0.65 (2.8)
(h) N. equatorial Africa	0.98 (3)	2.0 (1.7)	1.7 (1.6)
(i) S. equatorial Africa	0.41 (3)	0.65 (1.9)	0.64 (1.9)
(j) Central America	0.34 (3)	0.28 (2.0)	0.35 (2.2)
(k) S. America	0.77 (3)	0.81 (2.1)	1.0 (2.3)
(l) Australia	0.37 (3)	0.37 (2.5)	0.47 (2.3)
Global	5.3 (3)	9.4 (1.7)	8.9 (1.9)

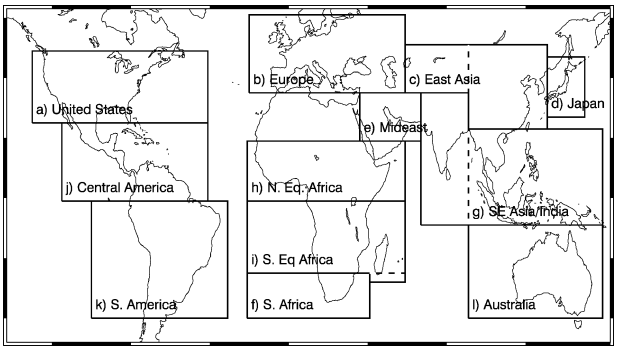

Fig. 1 Regions used in Tables 1–4 and Figs. 5 and 6.

conversion of slant tropospheric columns to vertical tropospheric columns and a 5×10^{14} molecules cm^{-2} absolute uncertainty due to spectral fitting. A detailed error analysis is provided by Martin *et al.*[18] Our relative error is slightly lower than the estimate given by Martin *et al.* because we have assumed random errors in spectral fitting, surface reflectivity and clouds. We do not use NO_2 columns poleward of 60° N, where the retrieval is sometimes more uncertain.

3.2. GOME NO_2 columns

The retrieved GOME tropospheric NO_2 columns are compared to modeled columns in Fig. 3. Monthly mean observed and modeled NO_2 columns are well correlated spatially and temporally ($r = 0.75$, $n = 149477$). Observations and model display enhanced NO_2 columns over the

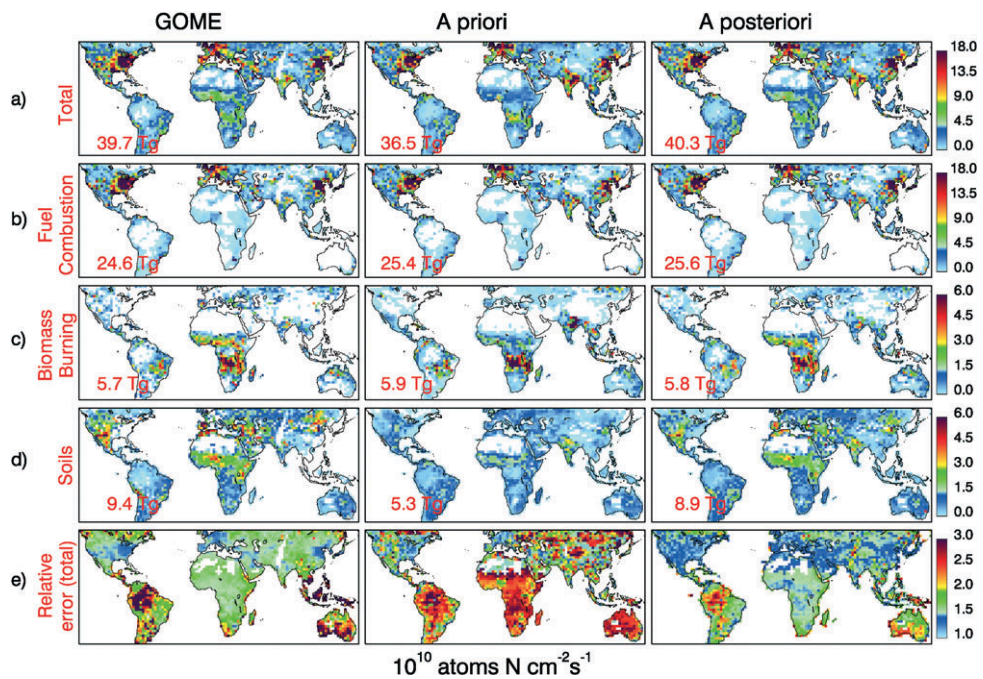

Fig. 2 Annual surface NO_x emissions for 2000: GOME top-down (left panels), *a priori* (middle panels) and *a posteriori* (right panels) inventories. Total surface NO_x emissions, shown on the top panels (a), are partitioned among: (b) fuel combustion, (c) biomass burning, and (d) soil emissions. All emissions are in 10^{10} atoms N cm^{-2} s^{-1} and the global annual emissions are indicated at the bottom left of each panel in TgN yr^{-1}. The bottom panels (e) display the relative errors (unitless) for total surface NO_x emissions.

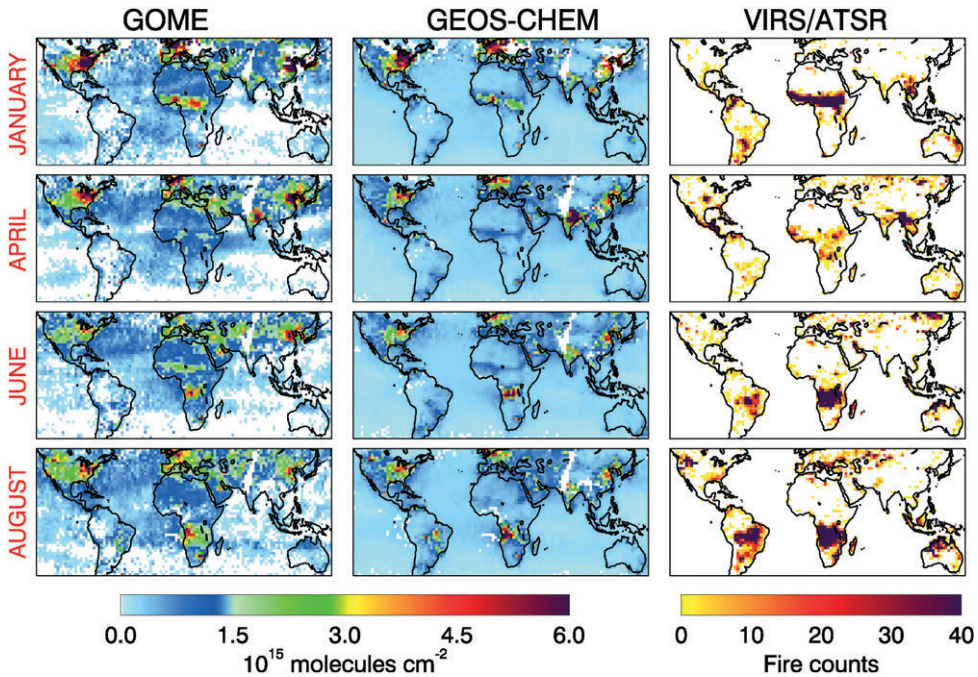

Fig. 3 Tropospheric NO_2 columns for January, April, June, and August 2000. Left panels: GOME observations. White areas indicate regions with no observations, or with cloud/snow cover >40%. Middle panels: GEOS-CHEM model results sampled at the GOME overpass time. Right panels: space-based observations of fires from VIRS[20] on board TRMM for the tropics (latitudes equatorward of 40°) and ATSR[21] on board ERS-2 at higher latitudes. All quantities are averaged over the GEOS-CHEM 2° × 2.5° horizontal grid.

industrialized regions of the eastern United States, Europe, India, East Asia, and South Africa throughout the year. Seasonal NO_x emissions from large-scale tropical fires can also be seen during the dry seasons in North equatorial Africa (January), India and Southeast Asia (April), South equatorial Africa (June and August), and to a smaller extent over South America (August). Note the increased NO_2 over Idaho and Montana in August 2000 due to unusually large wildfires.[19] The spatial location of these seasonal enhancements matches space-based active fire observations (Fig. 3, right panels) from the Visible and Infrared Scanner (VIRS) on board the Tropical Rainfall Measuring Mission satellite (TRMM).[20] The geographical coverage of VIRS fires spans tropical and subtropical latitudes (<40°). At higher latitudes, we supplement them with nighttime observations from the ATSR instrument[21] on board ERS-2.

During summer (Fig. 3, June and August), the GOME columns show regions of enhanced NO_2 in areas not associated with fuel combustion or biomass burning: the western United States, southern Europe, the Middle East, the African Sahel, and parts of East Asia. These enhancements are not captured by the model, and are consistent with larger than expected NO_x emissions from the seasonally dry soils in these regions.[7,8]

3.3. Global top-down NO_x inventory

The methodology to infer surface NO_x emissions from GOME NO_2 columns is based on inverse modeling with GEOS-CHEM, as described by Martin *et al.*,[7] linearly relating the observed NO_2 columns to NO_x emissions. The top-down emissions reflect surface NO_x emissions: GOME columns over land are relatively insensitive to lightning NO emissions because of the low densities and low NO_2/NO ratios in the upper troposphere.[7,8] Recent studies have found evidence for lightning signatures in GOME NO_2 columns over the Atlantic Ocean.[22–24] Transient lightning signals were also observed over North America away from surface NO_x sources.[22]

The main source of uncertainty in this inversion comes from the ability of the model to accurately simulate the lifetime of NO_x (*i.e.*, to simulate the partitioning between NO_x and total reactive nitrogen). This source of uncertainty was assessed to be less than 30%.[7] The overall uncertainty in the top-down emission inventory is 42% (obtained by adding in quadrature a 30% error from the model inversion and a 30% error from the NO_2 columns retrieval) which is combined with the 5×10^{14} molecules cm^{-2} absolute error. Our GOME inventory (with a global total of 40.5 TgN $year^{-1}$, Table 1 and Fig. 2) underestimates actual top-down NO_x emissions because of missing data caused by incomplete satellite sampling (for example over India) and areas with large cloud or snow cover (in particular during winter over eastern Europe, see Fig. 3). We assess this underestimate by sampling the *a priori* inventory only where GOME data is available, and find that 7% of total *a priori* emissions are thus missed. This observational undersampling will be corrected in the *a posteriori* inventory (section 4).

The top-down African emissions (6.9 TgN $year^{-1}$) are 10% lower than our previously published results (7.8 TgN $year^{-1}$), for the same GOME observations.[8] The difference comes from using a new GEOS-CHEM simulation for the inversion analysis, with improved isoprene emissions matching the seasonality inferred by GOME HCHO observations over Africa (Jaeglé *et al.*, manuscript in preparation).

3.4. Global partitioning of GOME top-down emissions

We derive the monthly partitioning of the top-down NO_x emissions (E) among fuel combustion (E_{FF+BF}), biomass burning (E_{BB}) and soils (E_{soil}), by combining *a priori* information on the spatial location of areas dominated by fuel combustion, together with space-based observations of fires. The block diagram on Fig. 4 illustrates the two-step approach we apply to each month and each $2^\circ \times 2.5^\circ$ grid box.

For grid boxes where *a priori* total emissions (E') are dominated by fuel combustion ($E'_{FF+BF}/E' > 0.9$) or where *a priori* combustion emissions exceed top-down emissions ($E'_{FF+BF} > E$), we assume that all top-down emissions are from fuel combustion ($E_{FF+BF} = E$, $E_{BB} = 0$, $E_{soil} = 0$). Elsewhere ($E'_{FF+BF}/E' \leq 0.9$ and $E'_{FF+BF} \leq E$) we set the top-down fuel combustion emissions to be

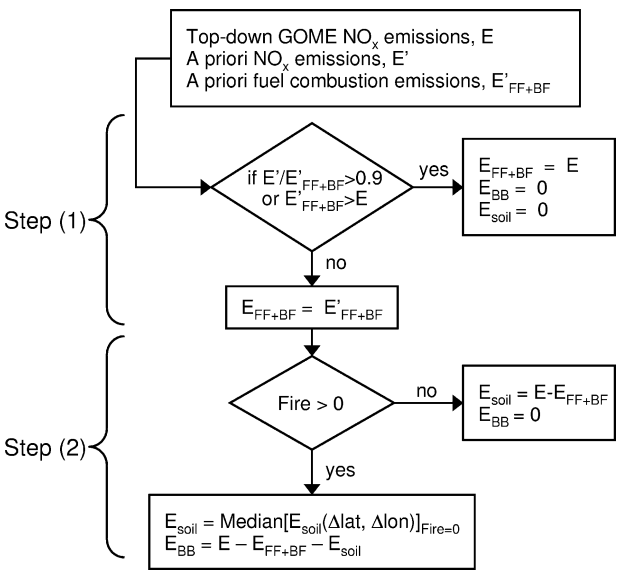

Fig. 4 Block diagram of algorithm applied to partition top-down GOME NO_x emissions (E) into: fuel combustion (E_{FF+BF}), biomass burning (E_{BB}) and soil (E_{soil}) emissions. The method is applied to monthly top-down NO_x emissions in each $2^\circ \times 2.5^\circ$ grid box, using information from the spatiotemporal distribution of bottom-up fuel combustion emissions (E'_{FF+BF}) and space-based fire count observations (Fire). See text (section 3.4) for detailed description.

equal to the *a priori* fuel combustion emissions ($E_{FF+BF} = E'_{FF+BF}$). This step thus takes advantage of the spatial separation between areas dominated by fuel combustion (northern hemisphere industrialized regions) and those dominated by soil or biomass burning (generally in the tropics).

Despite our use of the *a priori* in this first step, the large majority (80%) of the resulting GOME fuel combustion inventory is still determined by top-down emissions ($E_{FF+BF} = E$). This is because fuel combustion emissions are concentrated over small geographical areas where they dominate overall emissions; these regions are identified by our $E'_{FF+BF}/E' > 0.9$ condition and account for 76% of global GOME fuel combustion emissions. Regions where *a priori* combustion emissions exceed top-down emissions ($E'_{FF+BF} > E$) account for only 4% of GOME fuel combustion emissions and are located over SE Asia/India. The remaining 20% of top-down fuel combustion emissions are directly determined by the *a priori* ($E_{FF+BF} = E'_{FF+BF}$); these are mostly tropical regions with large soil or biomass burning emissions. We selected the $E'_{FF+BF}/E' > 0.9$ threshold by applying our algorithm to a synthetic inventory based on sampling the total *a priori* NO_x inventory only when GOME observations are available. With this threshold we were able to retrieve the original monthly regional *a priori* fuel combustion emissions to better than 2%, while at the same time minimizing the error from neglecting soil and biomass burning emissions in industrialized regions, and maximizing the fraction of fuel combustion emissions determined by the top-down inventory. Using the synthetic inventory we estimate that 7% (0.7%) of soil (biomass burning) emissions are located in areas with $E'_{FF+BF}/E' > 0.9$. This underestimate of soil emissions is corrected in the optimal combination of the *a priori* and top-down emissions inventories in section 4. Varying the threshold from 0.85 to 0.95 has a small effect our top-down retrieval of fuel combustion (less than 5%).

In the second step, we use monthly fire observations (*Fire*) to separate biomass burning from soil emissions. If no fires are detected in a grid box for a given month, we assign the residual top-down emissions to soils ($E_{soil} = E - E_{FF+BF}$, $E_{BB} = 0$). For each grid box where fires are detected (*Fire* > 0), we need to separate background soil emissions from biomass burning emissions. From our *a priori* inventory, we estimate that ~20–30% of emissions over biomass burning regions come from background soil emissions, which we thus need to take into account. This is achieved by calculating the median soil emissions in grid boxes within $\Delta lat = 6^\circ$ latitude and $\Delta lon = 10^\circ$ longitude where there are no fires:

$$\text{if } Fire[x,y] > 0 \text{ then } E_{soil}[x,y] = \text{Median}(E_{soil}[x',y']), \text{ for } Fire[x',y'] = 0 \text{ and } |x' - x| \le \Delta lon \text{ and } |y' - y| \le \Delta lat \quad (1)$$

where x (x') and y (y') are the longitude and latitude coordinates of the grid boxes with (without) fire. Once background soil emissions are determined, the residual is assigned to biomass burning ($E_{BB} = E - E_{FF+BF} - E_{soil}$).

The nighttime fire detection of ATSR likely undersamples tropical fires, which are characterized by a marked diurnal cycle.[25,26] In contrast, the orbit of TRMM permits the complete sampling of the diurnal burning cycle each month by VIRS.[20] In addition, the VIRS retrieval algorithm takes into account multiple satellite overpasses and cloud masking. We thus use VIRS observations where available (in the tropics and subtropics), and elsewhere we use ATSR observations. We eliminate false detections in ATSR due to oil and gas flaring.[27]

In this second step, the separation between emissions from soils and biomass burning relies only on the spatial distribution of observed fires and not on their intensity. This is an important point as comparisons among different remotely sensed biomass burning datasets have shown good agreement in identifying burning regions, but large disagreement in terms of the magnitude of the areas affected.[26,28–30] We test the sensitivity of our method to the choice of fire indicators by using ATSR everywhere or the Global Burned Area 2000 (GBA-2000) dataset from the SPOT VEGETATION sensor,[31] and find that our results are affected by less than 10%.

As described above, the robustness of our algorithm is assessed by applying it to partition a synthetic inventory based on the total *a priori* surface NO_x emissions. The original monthly regional *a priori* biomass burning and soil emissions are retrieved to within better than 10%, on average. We thus estimate relative errors in the individual top-down fuel combustion, soil, and biomass burning to be ~45% (including a 42% error from the top-down retrieval, 10% error from the partitioning algorithm, and 10% error from fire detection), which add to the absolute error.

4. *A posteriori* NO_x emissions

We combine the top-down NO_x emission inventory, E and its relative error ε, with *a priori* estimates from the bottom-up inventory, E' and its relative error ε', to obtain an *a posteriori* inventory, E''. If we assume a log-normal distribution of errors, the optimized inventory is obtained as[7]

$$\ln E'' = \frac{\ln E'(\ln \varepsilon)^2 + \ln E(\ln \varepsilon')^2}{(\ln \varepsilon)^2 + (\ln \varepsilon')^2} \quad (2)$$

with its relative error ε'' expressed as

$$\frac{1}{(\ln \varepsilon'')^2} = \frac{1}{(\ln \varepsilon)^2} + \frac{1}{(\ln \varepsilon')^2} \quad (3)$$

We also apply eqns. (2) and (3) to the fuel combustion and soil emissions to derive optimized *a posteriori* emissions, E''_{FF+BF} and E''_{soil}, and their respective relative errors, ε''_{FF+BF} and ε''_{soil}. Over areas where there are no GOME observations (section 3.3) or where top-down emissions are zero ($E_{soil} = 0$ or $E_{FF+BF} = 0$), we use the *a priori* and its associated relative errors instead. The optimized biomass burning inventory is inferred as the residual ($E''_{BB} = E'' - E''_{FF+BF} - E''_{soil}$).

The *a priori* and top-down relative errors for total NO_x emissions are generally comparable over source regions. The two inventories are thus given similar weights in the optimized inventory. The resulting *a posteriori* error is a factor of two lower compared to the *a priori* (Table 1 and Fig. 2). A similar reduction in the *a posteriori* error is found for the fuel combustion inventory. For soil and biomass burning emissions, the *a priori* relative errors (3) are much larger than the top-down errors (1.5–2), and thus the resulting *a posteriori* inventory is dominated by the top-down estimates of NO_x emissions. However, over areas where GOME observations are not available or top-down emissions are equal to zero, the *a posteriori* directly reflects the bottom-up inventory. Thus over regions with a significant fraction of missing data, *a posteriori* errors can sometimes be larger than the top-down errors (Tables 3 and 4).

5. Results

5.1. Fuel combustion emissions

The top-down GOME fuel combustion inventory is well correlated with the *a priori* inventory ($r = 0.85$, $n = 35160$), as shown in Fig. 2b. The GOME inventory (24.6 TgN year^{-1}) is 3% lower compared to the *a priori* (25.4 TgN year^{-1}). Over the United States, Europe and East Asia the two inventories agree to within 10%, lending confidence to our inversion and partitioning algorithm (Fig. 5 and Table 2). More pronounced differences are noted elsewhere: the GOME inventory is larger than the *a priori* over Japan (50%) and S. Africa (45%), but lower over SE Asia/India (−45%), Central America (−20%), South America (−30%) and Australia (−40%).

While the annual *a posteriori* and *a priori* fuel combustion emissions are very close to each other (25.6 TgN year^{-1} and 25.4 TgN year^{-1}, respectively), information from GOME has helped reduce the global annual errors by a factor of 2 (from ±80% to ±40%). The *a priori* and *a posteriori* fuel combustion inventories are very well correlated ($r = 0.96$, $n = 35\,160$). Regionally, the *a posteriori* is within 10% of the *a priori*, with the exception of Japan and S. Africa where the *a posteriori* is larger by 25%. Regions of disagreement where the top-down inventory was lower than the *a priori* were caused by under sampling by GOME (section 3.3) and disappear in the *a posteriori*. The fuel combustion inventory from EDGAR[16] (26.1 TgN year^{-1}) is also very similar to our *a priori* and *a posteriori* inventories (Table 2 and Fig. 5). The largest differences are for Europe and the Middle East, where EDGAR emissions are 37% larger and 33% lower than the *a posteriori*, respectively.

The monthly *a posteriori* fuel combustion emissions are aseasonal over most regions, with the exception of Europe and East Asia (Fig. 6, grey bars). Our *a priori* fuel combustion inventory does not include any seasonality over East Asia. However the *a posteriori* inventory suggests larger fuel combustion emissions during the winter months. The ratio of monthly emissions in December (maximum) to emissions in July (minimum) is 1.4. Streets *et al.*[32] examined the potential seasonality of Chinese NO_x emissions due to heating in homes, assuming a dependence of stove operation on

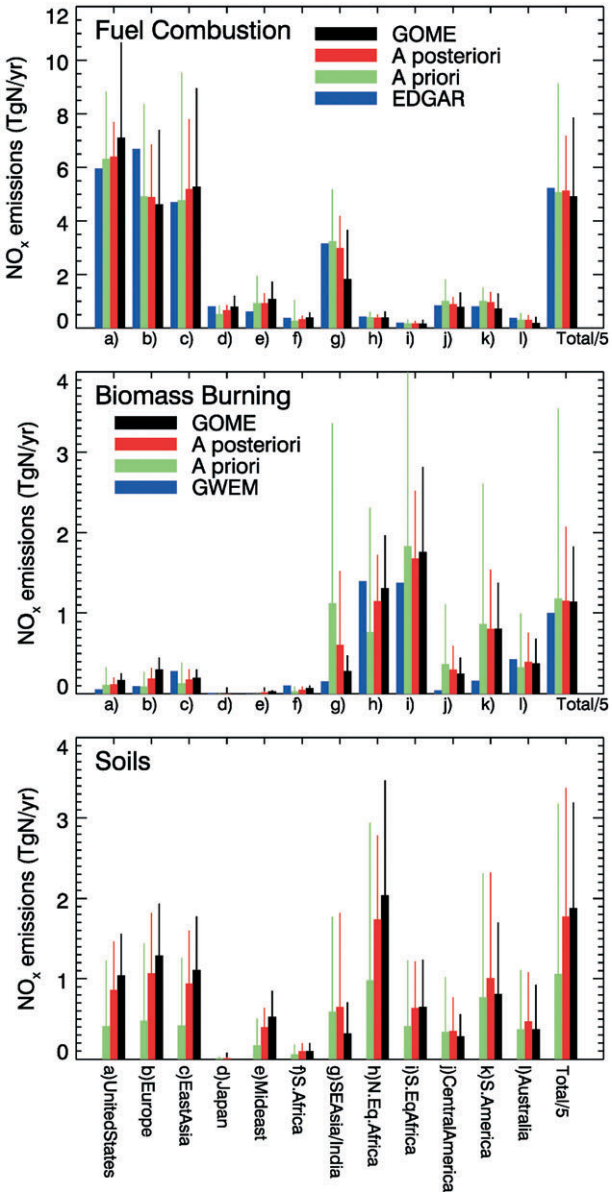

Fig. 5 Regional GOME top-down (black), *a priori* (green), and *a posteriori* (red) annual NO_x emissions in TgN $year^{-1}$ for 2000: (top panel) fuel combustion emissions, (middle panel) biomass burning, and (bottom panel) soil emissions. The thin lines on top of each bar displays the absolute errors. Note that global emissions (rightmost bars) are divided by a factor of 5. Also shown are the inventories from EDGAR[16] for fuel combustion (blue bars on top panel) and GWEM[41] for biomass burning (blue bars on middle panel). The geographical definition of each region is displayed on Fig. 1.

outdoor temperature, and estimated a 1.2 ratio between maximum and minimum fuel combustion emissions. Their calculation neglected seasonality in power generation and industrial energy use, which are also likely to vary seasonally. Over Europe we derive a ratio between maximum and minimum emissions of 1.3, similar to seasonality in the *a priori*, which is due to wintertime heating.

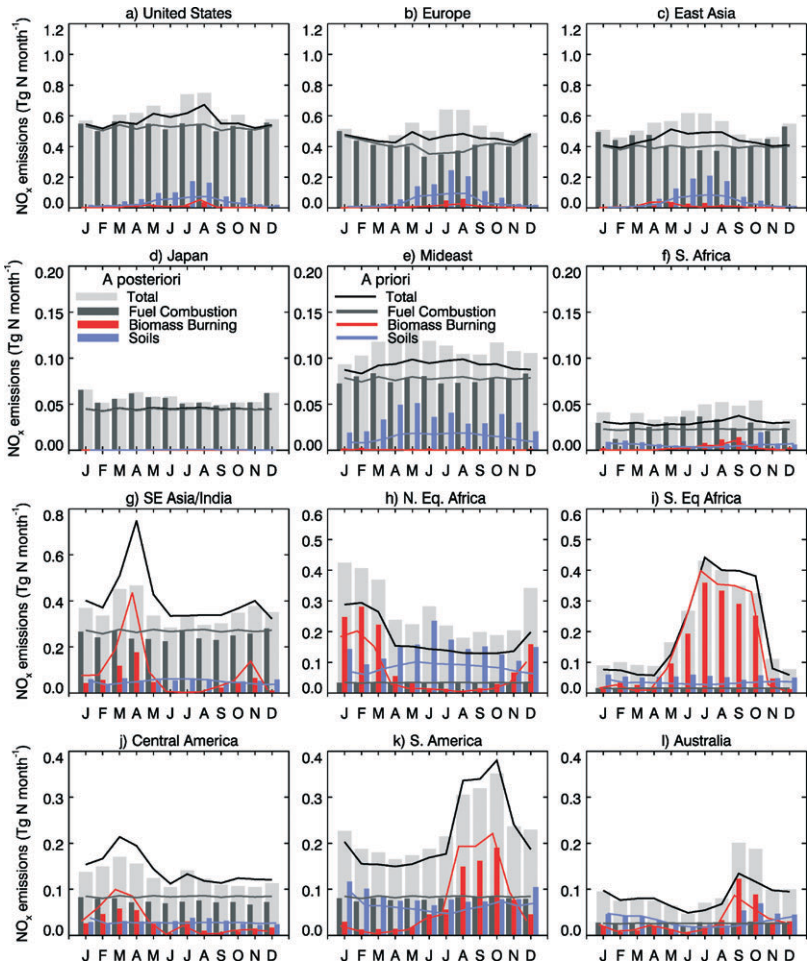

Fig. 6 Monthly regional *a posteriori* (bars) and *a priori* (lines) NO_x emissions in 2000. We show total emissions (light grey bars for *a posteriori* and black line for *a priori*) as well as their partitioning among fuel combustion (dark grey), biomass burning (red), and soil emissions (blue). Note the change in scales for the panels on each row.

5.2. Biomass burning emissions

The global annual biomass burning inventories for the *a priori* (5.9 TgN $year^{-1}$), top-down (5.7 TgN $year^{-1}$) and *a posteriori* (5.8 TgN $year^{-1}$) are nearly identical, but the inclusion of GOME observations greatly reduces errors, from ±200% to ±80%. There is good spatial and temporal correlation among these inventories ($r = 0.69$ for GOME *vs. a priori*; $r = 0.85$ for *a posteriori vs. a priori*, $n = 35\,160$). Regionally the largest differences are for SE Asia/India, where the *a posteriori* (0.6 TgN $year^{-1}$) is 46% lower than the *a priori* (1.1 TgN $year^{-1}$), and for North equatorial Africa, where the *a posteriori* (1.2 TgN $year^{-1}$) is 50% larger than the *a priori* (0.77 TgN $year^{-1}$) (Table 3 and Fig. 5). For North equatorial Africa, the underestimate of the *a priori* is likely a result of an underestimate of the NO emission factor (EF = 1.1 (g NO) $(kg\ dry\ matter)^{-1}$) used in our inventory for North African savannas.[7,8] Over South equatorial Africa, where we use a higher EF (3.9 g kg^{-1}),[33] there is closer agreement between the *a priori* (1.8 TgN $year^{-1}$) and the *a posteriori* (1.7 TgN $year^{-1}$). Overall, fires over Africa account for half of the global biomass burning emissions. Globally, biomass burning emissions contribute 14% of surface NO_x emissions.

The *a priori* and *a posteriori* display similar seasonality over the major biomass burning regions, with maximum emissions in February for North equatorial Africa, March for Central America, April for SE Asia/India, July in South equatorial Africa, September in Australia and October in South America (Fig. 6, compare red bars and red lines). This good agreement on the seasonal cycle of burning validates the approach used by Duncan *et al.*[12] to specify seasonal variations in the *a priori*, *via* regional scaling of a bottom-up inventory with fire count and aerosol satellite observations.

5.3. Soil emissions

Globally, our top-down soil emissions (9.4 TgN year^{-1}) are 77% larger than the *a priori* (5.3 TgN year^{-1}); the *a posteriori* soil emissions (8.9 TgN year^{-1}) are 68% larger than the *a priori*. The spatial distribution of our inferred annual soil emissions corresponds well to the *a priori* ($r = 0.51$, $n = 2349$ for GOME *vs*. *a priori*; $r = 0.79$, $n = 2741$ for *a posteriori vs*. *a priori*). The large underestimate of soil emissions by the *a priori* appears to be systematic for all regions (see Fig. 5, bottom panel, and Table 4), and is especially strong during the summer over mid-latitude regions and during the wet season in the Tropics (Fig. 6).

North equatorial Africa is identified as having large soil emissions (Fig. 2, Table 4). We previously argued that these NO_x emissions are due to rain-induced pulsing from soils over vast areas of the Sahel.[8] Many field and laboratory experiments have reported large pulses of biogenic NO emissions following rain on dry soils of savannas and seasonally dry forests.[34–38] We found that the spatial and temporal distribution of the GOME NO_2 enhancements over Africa is consistent with soil NO emissions from ecosystem-dependent flux measurements[39] and from surface measurements of NO_2 obtained by the IDAF (IGAC/DEBITS/Africa) network over West Africa. We showed that lightning and clouds are unlikely to account for the enhanced GOME NO_2 columns and IDAF surface NO_2 observations.

Here we see that the large inferred soil emissions are not restricted to the tropics, but extend to mid-latitude regions as well. In particular, our *a posteriori* analysis indicates a factor of two increase in soil emissions over Europe, the US and East Asia (Fig. 5, Table 4).

6. Comparison of *a posteriori* to previous studies

Table 1 compares our 2000 *a posteriori* inventory with the *a posteriori* inventory of Martin *et al.*,[7] based on GOME observations for September 1996–August 1997. Our global *a posteriori* NO_x source is 7% larger than their 37.8 TgN year^{-1} *a posteriori* source. Most of the difference is for Tropical regions and could reflect interannual variations in biomass burning.

Müller and Stavrakou[40] used an adjoint modeling technique based on the IMAGES model to derive an optimized NO_x emission inventory using GOME NO_2 columns for 1997, as well as surface observations of CO. Their inversion resulted in a 38.7 TgN year^{-1} annual surface NO_x emissions, which is close to our *a posteriori* estimate of 40.3 TgN year^{-1}. Their global fuel combustion source (22.8 TgN year^{-1}) and biomass burning source (4.4 TgN year^{-1}) are 11% and 24% lower than our *a posteriori*, respectively. In agreement with our results, they infer a strong role for soil NO_x emissions, with even larger global emissions (12.1 TgN year^{-1}). Their NO_x emissions over North America, Europe and South Asia (8.3, 5, 5.2 TgN year^{-1}) are similar to our results (7.8, 4.9, 5.6 TgN year^{-1} – using the same regional definitions). However, they infer larger sources over S. America and Africa (6.1 and 8.8 TgN year^{-1}) compared to our study (4.3 and 7 TgN year^{-1}). While our study generally agrees with the results of Müller and Stavrakou,[40] some of the discrepancies noted above are likely the results of differences in: *a priori* emissions (IMAGES uses larger *a priori* fuel combustion and soil NO_x emissions), years, retrieval approaches for the GOME NO_2 columns, and chemical mechanisms used in the inversions.

6.1. Biomass burning emissions

Table 3 and Fig. 5 compares our *a posteriori* biomass burning estimate with the Global Wildland Fire Emission Model 1.4 (GWEM) inventory of Hoelzemann.[41] This inventory is an improvement of an earlier inventory (GWEM 1.21).[42] It is based on the GBA-2000 burned area product (with the

exception of S. America where GOES and AVHRR fire counts are used) and fuel loads from the LPJ-DGVM model. These inventories are in broad agreement, with the GWEM global inventory (5 TgN $year^{-1}$) being 13% lower than our *a posteriori* (5.8 TgN $year^{-1}$). We note that the GWEM inventory does not include seasonal emissions from burning of agricultural residues in the field, while our biomass burning inventories take this source into account. Open field agricultural residue burning produces 0.2 TgN $year^{-1}$, as derived in the inventory of Logan and Yevich[10] (which is used in our *a priori*), and is thus unlikely to fully account for the differences between GWEM and our inventory.

Biomass burning estimates from GWEM and our *a posteriori* are lower than some of the earlier studies. For example the climatological emission inventory of Galanter *et al.*[43] yields 7.8 TgN $year^{-1}$. The Schultz[27] inventory for 2000 yields 7.5 TgN $year^{-1}$.

Both GWEM and *a posteriori* estimates display reduced emissions over SE Asia/India relative to the *a priori*, by 86% and 46%, respectively. Similar conclusions were reached by previous studies based on inverse modeling analyses of CO observations.[44,45] Our *a posteriori* estimates for biomass burning emissions of NO_x over Asia (0.8 TgN $year^{-1}$) agrees with estimates from a recent bottom-up inventory by Streets *et al.*[46] (0.85 TgN $year^{-1}$). The convergence towards lower biomass burning emissions over Asia is likely to be due to an overestimate in the amount of biomass burnt used in early studies, especially over India.[46]

For the African continent (south of the Sahara), the GWEM inventory and our *a posteriori* both estimate 2.9 TgN $year^{-1}$ for NO_x emissions. However, while in GWEM African emissions north and south of the equator are nearly equal, in our *a posteriori* we find that burning south of the equator is 40% larger than north of the equator. For comparison, Barbosa *et al.*[47] estimate NO_x emissions from vegetation fires of 1.2–4.5 TgN $year^{-1}$ over Africa during the 1980s, while Scholes and Andreae[48] find 2.8 TgN $year^{-1}$, similar to our estimates.

The largest difference between GWEM and our *a posteriori* occurs over South and Central America, which account for 0.2 TgN $year^{-1}$ in GWEM compared to 1.1 TgN $year^{-1}$ in the *a posteriori*. Our *a posteriori* contains large uncertainties over this region because of the South Atlantic anomaly.[49] However, burned areas in South America are probably underestimated in GWEM (J. Hoelzemann, personal communication), because with its 4 km resolution the GOES fire product might not detect many tropical deforestation fires, which typically cover small areas (0.2–1 km^2).[50] In comparison, Potter *et al.*[51] find that deforestation fires over the Amazon in the early 1990s resulted in 1.6 TgN $year^{-1}$.

In addition to the GWEM inventory, two other global studies (van der Werf *et al.*[52] and Ito and Penner[53]) have estimated trace gas emissions from biomass burning during 2000 based on remote sensing of burned areas and active fires. NO_x emissions have not been reported from these other two inventories. However, comparisons of the carbon emissions for these three studies show significant differences,[28] with global emissions ranging from 1428 TgC to 2600 TgC, African emissions ranging from 880 TgC to 1880 TgC, and South/Central American emissions ranging from 90 TgC $year^{-1}$ to 760 TgC $year^{-1}$. This range reflects highly different estimates of both burned areas[29,54] and available fuel loads.[28] Given such difficulties in relating space-based observations of active fires and burned areas to gas emissions, we propose that our *a posteriori* biomass burning inventory could provide a way to independently validate the algorithms used in these recent studies for the year 2000.

6.2. Asian fuel combustion emissions

Our *a posteriori* estimate for fuel combustion over Asia (8.8 TgN $year^{-1}$, including East Asia, SE Asia/India and Japan) is 28% larger than the bottom-up inventory of Streets *et al.*[32] (6.9 TgN $year^{-1}$). The largest discrepancies are for China and India, where our fuel combustion emissions (4.4 TgN $year^{-1}$ and 1.7 TgN $year^{-1}$) are 38% and 43% higher than the Streets *et al.* inventory, respectively. Modeling analyses based on CO observations by aircraft and satellite observations during the TRACE-P field mission[44,45,55,56] also found that the Streets *et al.* inventory significantly underestimates anthropogenic emissions over China. Causes for this underestimate could include under-reporting of domestic coal burning[32,56] or inefficient industrial sources and power plants.[57]

In an inverse modeling study using NO_y *in situ* observations, Wang *et al.*[58] inferred a 47% increase in Chinese NO_x emissions, relative to the Streets *et al.* inventory. They estimate a 5 TgN $year^{-1}$ total NO_x source for China, which is close to our total *a posteriori* source (5.3 TgN $year^{-1}$).

6.3. Soil emissions

The global magnitude of soil-atmospheric NO_x exchange has been challenging to constrain because of the large spatiotemporal variability of microbial soil processes,[59,60] the influence of human activities[61] such as N-fertilization[62] and burning[37] in enhancing soil emissions, and the role of plant canopies in recapturing a significant fraction of the emitted soil NO_x.[63,64] The most recent global soil inventories include the semi-empirical model of Yienger and Levy[14] (used in our *a priori*), the process-based land-vegetation biogeochemistry model of Potter *et al.*,[65] and the inventory of Davidson and Kingerlee[66] based on global extrapolations of surface flux measurements. The above-canopy soil emissions derived by Yienger and Levy and Potter *et al.* (5.5 and 5 TgN $year^{-1}$, respectively) are a factor of two lower than the results of Davidson and Kingerlee (13 TgN $year^{-1}$). The global soil NO_x estimate from our *a posteriori*, with 8.9 TgN $year^{-1}$, is in between these two values. By construction, our *a posteriori* estimate depends on the *a priori*. We conducted a sensitivity study where we doubled the *a priori* soil emissions, and derived an *a posteriori* value of 10.4 TgN $year^{-1}$ for soil emissions, closer to values obtained by Davidson and Kingerlee and by Müller and Stavrakou[40] in their inversion analysis.

The largest biogenic emissions of NO_x have been measured from fertilized agriculture and seasonally dry tropical ecosystems.[66] These systems support rapid nitrogen cycling (*via* nitrification and denitrification), high temperatures, and/or seasonally low moisture. Consistent with these field measurements, our study highlights the role of tropical savanna/woodland ecosystems as a large source of NO_x. We also find large emissions from mid-latitude grassland and cropland areas during summer, especially over the western US (Great Plains), southern Europe (Spain, Greece, Turkey), China, and India (Fig. 2).

Africa accounts for nearly 30% of our global *a posteriori* soil emissions. These emissions peak at the beginning of the rainy season, in June (Fig. 6h). The difference between our *a posteriori* and the *a priori* during the rainy season suggests that the Yienger and Levy algorithm underestimates the magnitude of rain-induced pulsing.[8]

Relative to the *a priori* inventory, we find a larger increase in northern mid-latitude soil emissions (25° N–60° N: 1.7 TgN $year^{-1}$ *a priori*, compared to 3.9 TgN $year^{-1}$ in *a posteriori*) than in the tropical emissions (25° S–25° N: 3 TgN $year^{-1}$ *a priori*, compared to 4.3 TgN $year^{-1}$ in *a posteriori*). This larger role for mid-latitude emissions could reflect a strong source of NO_x from fertilized agricultural soils. Global estimates of soil emissions from agricultural fields and the effect of nitrogen fertilization vary widely, ranging from 0.5 to 3 TgN $year^{-1}$[14,62,67,68] (not including canopy recapture). Including the canopy recapture of Yienger and Levy, these numbers range from 0.4 to 2.25 TgN $year^{-1}$. The main uncertainty in these estimates comes from assessing the fraction of applied N-fertilizer released as NO, which vary from 0.3%[62] at the low end, to 2.5%[14] at the high end of these compilations. By multiplying the area of cropland by an average annual emission flux based on observations, Davidson and Kingerlee estimate an even larger source of 5.4 TgN $year^{-1}$ (3.9 TgN $year^{-1}$ with canopy recapture).

We estimate the role of emissions from agricultural fields by scaling our *a posteriori* soil emissions by the fraction of emissions coming from agriculture. Yienger and Levy find that 75% of emissions from temperate soils and 25% of emissions from tropical soils come from agriculture, while in Davidson and Kingerlee these numbers are 21% and 28%. We thus find that, globally, 2.5–4.5 TgN $year^{-1}$ are emitted by N-fertilized soils: with 1.1–1.6 TgN $year^{-1}$ in the Tropics and 0.9–3.4 TgN $year^{-1}$ in the extratropics. These numbers are at the upper end of the previous estimates listed above. Asia contains one third of the world's total cropland area and accounts for more than half of the global N-fertilizer consumption,[69] with China and India being the largest users. Indeed, our *a posteriori* soil emissions are highest over the North China Plain and North India (Fig. 2), which are regions with extensive croplands and where chemical N-fertilizers are heavily used. In their inversion study for Asia, Wang *et al.*[58] proposed that decomposition of organic wastes and extensive applications of chemical fertilizer could account for 1.1 TgN $year^{-1}$ over China alone. This is consistent with our *a posteriori* estimate of $\sim$1 TgN $year^{-1}$ from soil emissions over East Asia. In contrast, by using a bottom-up approach, Yan *et al.*[67] estimate that only 0.2 TgN $year^{-1}$ are emitted from croplands in China. These discrepancies clearly warrant a close re-examination of fertilizer-induced NO_x release.

Globally, soil emissions account for 22% of NO_x emissions in our *a posteriori* inventory, but only 14% of the *a priori*. The *a posteriori* indicates that in the Tropics, soil emissions (4.3 TgN $year^{-1}$) are

comparable to biomass burning emissions (4.7 TgN year^{-1}), while in the *a priori* soil emissions (3 TgN year^{-1}) are 40% lower than biomass burning (5 TgN year^{-1}). In addition, we infer a large role for soil emissions at northern mid-latitudes during summer (June–August), where they account for nearly half that of the fuel combustion source (compared to only 20% in the *a priori*). This suggests that the current generation of global and regional chemical transport models (which generally use low estimates of soil emissions) likely underestimate the role of biogenic emissions in controlling background levels of ozone, especially during the rainy season in the Tropics and during summer for northern mid-latitudes.

7. Conclusions

We have presented a simple method to partition global NO_x emissions derived from the Global Ozone Monitoring Experiment (GOME) into fuel combustion, biomass burning and soil emissions for the year 2000. Our resulting *a posteriori* fuel combustion emissions (25.6 TgN year^{-1}) are very close to the GEIA-based *a priori* (25.4 TgN year^{-1}), lending confidence to our separation method, and errors are reduced by a factor of two from $\pm$80% to $\pm$40%. Fuel combustion emissions are aseasonal, with the exception of Europe and East Asia.

The global *a posteriori* estimate of biomass burning emissions (5.8 TgN year^{-1}) is similar to the *a priori* (5.9 TgN year^{-1}), with a significant decrease in the uncertainty from $\pm$200 to $\pm$80%. The *a posteriori* estimate of NO_x emissions from SE Asia/India is decreased by 46% relative to the *a priori*, similar to the results of previous studies based on inverse modeling analyses of CO observations. Over North equatorial Africa, *a posteriori* emissions are 50% larger than the *a priori*, likely due to errors in the NO_x emission factor used in the *a priori*. We propose that our *a posteriori* biomass burning inventory can be used to validate independent bottom-up estimates of fire emissions based on remote sensing of burned areas and active fires for 2000.

We find a 68% increase in soil emissions from 5.3 TgN year^{-1} to 8.9 TgN year^{-1}. The *a posteriori* inventory displays the largest soil emissions over tropical savanna/woodland ecosystems during the wet season, as well as over agricultural regions in mid-latitudes during summer. We estimate that 2.5–4.5 TgN year^{-1} are emitted by N-fertilized soils, at the upper end of previous estimates. The large underestimate of atmospheric-soil NO_x exchange by the Yienger and Levy[14] algorithm used in our *a priori*, appears to reflect an underestimate of N-fertilized NO release from croplands as well as an underestimate of rain-induced pulsing from semiarid soils. This points to a clear need to better constrain these two effects, and re-evaluate the role of soil emissions in controlling background ozone levels.

Acknowledgements

This work was supported by funding from the NASA New Investigator Program in Earth Science (NAG5-10637). The GEOS-CHEM model is managed by the Atmospheric Chemistry Modeling group at Harvard University with support from the NASA Atmospheric Chemistry Modeling and Analysis Program. We thank J. Hoelzemann for providing us with the gridded GWEM 1.4 inventory.

References

1 M. J. Prather and D. Ehhalt, in *Climate Change 2001: The Science of Climate Change, Intergovernmental Panel on Climate Change*, Cambridge University Press, Cambridge, 2001, p. 241.
2 J. A. Logan, *J. Geophys. Res.*, 1983, **88**, 785.
3 E. A. Holland, F. J. Dentener, B. H. Braswell and J. M. Sulzman, *Biogeochemistry*, 1999, **46**, 7.
4 ESA, *The GOME users manual, ESTEC, European Space Agency Publication SP-1182*, ESA Publications Division, Noordwijk, The Netherlands, 1995, ISBN-92-9092-327-x.
5 J. P. Burrows, M. Weber, M. Buchwitz, V. Rozanov, A. Ladstatter-Weissenmayer, A. Richter, R. DeBeek, R. Hoogen, K. Bramstedt, K. U. Eichmann and M. Eisinger, *J. Atmos. Sci.*, 1999, **56**, 151.
6 C. Leue, M. Wenig, T. Wagner, O. Klimm, U. Platt and B. Jahne, *J. Geophys. Res.*, 2001, **106**, 5493.
7 R. V. Martin, D. J. Jacob, K. Chance, T. P. Kurosu, P. I. Palmer and M. J. Evans, *J. Geophys. Res.*, 2003, **108**, DOI: 10.1029/2003JD003453.
8 L. Jaeglé, R. V. Martin, K. Chance, L. Steinberger, T. P. Kurosu, D. J. Jacob, A. I. Modi, V. Yoboué, L. Sigha-Nkamdjou and C. Galy-Lacaux, *J. Geophys. Res.*, 2004, **109**, DOI: 10.1029/2004JD004787.

9 I. Bey, D. J. Jacob, R. M. Yantosca, J. A. Logan, B. D. Field, A. M. Fiore, Q. B. Li, H. G. Y. Liu, L. J. Mickley and M. G. Schultz, *J. Geophys. Res.*, 2001, **106**, 23073.
10 R. Yevich and J. A. Logan, *Global Biogeochem. Cycles*, 2003, **17**, DOI: 10.1029/2002GB001952.
11 J. M. Lobert, W. C. Keene, J. A. Logan and R. Yevich, *J. Geophys. Res.*, 1999, **104**, 8373.
12 B. N. Duncan, R. V. Martin, A. C. Staudt, R. Yevich and J. A. Logan, *J. Geophys. Res.*, 2003, **108**, DOI: 10.1029/2002JD002378.
13 C. M. Benkovitz, M. T. Scholtz, J. Pacyna, L. Tarrason, J. Dignon, E. C. Voldner, P. A. Spiro, J. A. Logan and T. E. Graedel, *J. Geophys. Res.*, 1996, **101**, 29239.
14 J. J. Yienger and H. Levy, *J. Geophys. Res.*, 1995, **100**, 11447.
15 Y. H. Wang, D. J. Jacob and J. A. Logan, *J. Geophys. Res.*, 1998, **103**, 10713.
16 J. G. J. Olivier and J. J. M. Berdowski, in *The Climate System*, ed. J. Berdowski, R. Guicherit and B.J. Heij, AA Balkema Publishers, Lisse, The Netherlands, 2001, p. 33.
17 K. Chance, P. I. Palmer, R. J. D. Spurr, R. V. Martin, T. P. Kurosu and D. J. Jacob, *Geophys. Res. Lett.*, 2000, **27**, 3461.
18 R. V. Martin, K. Chance, D. J. Jacob, T. P. Kurosu, R. J. D. Spurr, E. Bucsela, J. F. Gleason, P. I. Palmer, I. Bey, A. M. Fiore, Q. B. Li, R. M. Yantosca and R. B. A. Koelemeijer, *J. Geophys. Res.*, 2002, **107**, DOI: 10.1029/2001JD002622.
19 J. F. Lamarque, D. P. Edwards, L. K. Emmons, J. C. Gille, O. Wilhelmi, C. Gerbig, D. Prevedel, M. N. Deeter, J. Warner, D. C. Ziskin, B. Khattatov, G. L. Francis, V. Yudin, S. Ho, D. Mao, J. Chen and J. R. Drummond, *Geophys. Res. Lett.*, 2003, **30**, DOI: 10.1029/2003GL017503.
20 L. Giglio, J. D. Kendall and R. Mack, *Int. J. Remote Sens.*, 2003, **24**, 4505.
21 O. Arino and J. M. Melinotte, *Int. J. Remote Sens.*, 1998, **19**, 2019.
22 Y. Choi, Y. H. Wang, T. Zeng, R. V. Martin, T. P. Kurosu and K. Chance, *Geophys. Res. Lett.*, 2005, in press.
23 A. Richter and J. P. Burrows, *Adv. Space Res.*, 2002, **29**, 1673.
24 D. P. Edwards, J. F. Lamarque, J. L. Attie, L. K. Emmons, A. Richter, J. P. Cammas, J. C. Gille, G. L. Francis, M. N. Deeter, J. Warner, D. C. Ziskin, L. V. Lyjak, J. R. Drummond and J. P. Burrows, *J. Geophys. Res.*, 2003, **108**, DOI: 10.1029/2002JD002927.
25 S. Langaas, *Nature*, 1993, **363**, 120.
26 H. Eva and E. F. Lambin, *Remote Sens. Environ.*, 1998, **64**, 292.
27 M. G. Schultz, *Atmos. Chem. Phys.*, 2002, **2**, 387.
28 E. S. Kasischke and J. E. Penner, *J. Geophys. Res.*, 2004, **109**, doi:10.1029/2004JD004972.
29 L. Boschetti, H. D. Eva, P. A. Brivio and J. M. Grégoire, *Geophys. Res. Lett.*, 2004, **31**, DOI: 10.1029/2004GL021229.
30 M. Simon, S. Plummer, F. Fierens, J. J. Hoelzemann and O. Arino, *J. Geophys. Res.*, 2004, **109**, DOI: 10.1029/2003JD003622.
31 J. M. Grégoire, K. Tansey and J. M. N. Silva, *Int. J. Remote Sens.*, 2003, **24**, 1369.
32 D. G. Streets, T. C. Bond, G. R. Carmichael, S. D. Fernandes, Q. Fu, D. He, Z. Klimont, S. M. Nelson, N. Y. Tsai, M. Q. Wang, J. H. Woo and K. F. Yarber, *J. Geophys. Res.*, 2003, **108**, DOI: 10.1029/2002JD003093.
33 M. O. Andreae and P. Merlet, *Global Biogeochem. Cycles*, 2001, **15**, 955.
34 C. Johansson and E. Sanhueza, *J. Geophys. Res.*, 1988, **93**, 14193.
35 E. A. Davidson, *Soil Sci. Soc. Am. J.*, 1992, **56**, 95.
36 G. W. Harris, F. G. Wienhold and T. Zenker, *J. Geophys. Res.*, 1996, **101**, 23707.
37 J. S. Levine, E. L. Winstead, D. A. B. Parsons, M. C. Scholes, R. J. Scholes, W. R. Cofer, D. R. Cahoon and D. I. Sebacher, *J. Geophys. Res.*, 1996, **101**, 23689.
38 M. C. Scholes, R. Martin, R. J. Scholes, D. Parsons and E. Winstead, *Nutr. Cycl. Agroecosyst.*, 1997, **48**, 115.
39 D. Serça, R. Delmas, X. Le Roux, D. A. B. Parsons, M. C. Scholes, L. Abbadie, R. Lensi, O. Ronce and L. Labroue, *Global Biogeochem. Cycles*, 1998, **12**, 637.
40 J. F. Müller and T. Stavrakou, *Atmos. Chem. Phys. Disc.*, 2005, **4**, 7985.
41 J. J. Hoelzemann, *Global wildland fire emission modeling: Assessing variability of emissions and their impact on atmospheric chemistry*, PhD thesis, Max Planck Institute for Meteorology, Hamburg, 2005.
42 J. J. Hoelzemann, M. G. Schultz, G. P. Brasseur, C. Granier and M. Simon, *J. Geophys. Res.*, 2004, **109**, DOI: 10.1029/2003JD003666.
43 M. Galanter, H. Levy and G. R. Carmichael, *J. Geophys. Res.*, 2000, **105**, 6633.
44 P. I. Palmer, D. J. Jacob, D. B. A. Jones, C. L. Heald, R. M. Yantosca, J. A. Logan, G. W. Sachse and D. G. Streets, *J. Geophys. Res.*, 2003, **108**, DOI: 10.1029/2003JD003397.
45 C. L. Heald, D. J. Jacob, D. B. A. Jones, P. I. Palmer, J. A. Logan, D. G. Streets, G. W. Sachse, J. C. Gille, R. N. Hoffman and T. Nehrkorn, *J. Geophys. Res.*, 2004, **109**, DOI: 10.1029/2004JD005185.
46 D. G. Streets, K. F. Yarber, J. H. Woo and G. R. Carmichael, *Global Biogeochem. Cycles*, 2003, **17**, doi:10.1029/2003GB002040.
47 P. M. Barbosa, D. Stroppiana, J. M. Gregoire and J. M. C. Pereira, *Global Biogeochem. Cycles*, 1999, **13**, 933.
48 M. Scholes and M. O. Andreae, *Ambio*, 2000, **29**, 23.

49 J. R. Heirtzler, *J. Atmos. Sol. Terr. Phys.*, 2002, **64**, 1701.
50 Y. J. Kaufman, P. V. Hobbs, V. Kirchhoff, P. Artaxo, L. A. Remer, B. N. Holben, M. D. King, D. E. Ward, E. M. Prins, K. M. Longo, L. F. Mattos, C. A. Nobre, J. D. Spinhirne, Q. Ji, A. M. Thompson, J. F. Gleason, S. A. Christopher and S. C. Tsay, *J. Geophys. Res.*, 1998, **103**, 31783.
51 C. Potter, V. Brooks-Genovese, S. Klooster and A. Torregrosa, *J. Geophys. Res.*, 2002, **107**, DOI: 10.1029/2000JD000250.
52 G. R. van der Werf, J. T. Randerson, G. J. Collatz, L. Giglio, P. S. Kasibhatla, A. F. Arellano, S. C. Olsen and E. S. Kasischke, *Science*, 2004, **303**, 73.
53 A. Ito and J. E. Penner, *J. Geophys. Res.*, 2004, **109**, DOI: 10.1029/2003JD004423.
54 K. Tansey, J. M. Grégoire, D. Stroppiana, A. Sousa, J. Silva, J. M. C. Pereira, L. Boschetti, M. Maggi, P. A. Brivio, R. Fraser, S. Flasse, D. Ershov, E. Binaghi, D. Graetz and P. Peduzzi, *J. Geophys. Res.*, 2004, **109**, DOI: 10.1029/2003JD003598.
55 D. Allen and K. Pickering, and M. Fox-Rabinovitz, *J. Geophys. Res.*, 2004, **109**, DOI: 10.1029/2003JD004250.
56 G. R. Carmichael, Y. Tang, G. Kurata, I. Uno, D. G. Streets, N. Thongboonchoo, J. H. Woo, S. Guttikunda, A. White, T. Wang, D. R. Blake, E. Atlas, A. Fried, B. Potter, M. A. Avery, G. W. Sachse, S. T. Sandholm, Y. Kondo, R. W. Talbot, A. Bandy, D. Thorton and A. D. Clarke, *J. Geophys. Res.*, 2003, **108**, DOI: 10.1029/2002JD003116.
57 P. Suntharalingam, D. J. Jacob, P. I. Palmer, J. A. Logan, R. M. Yantosca, Y. P. Xiao, M. J. Evans, D. G. Streets, S. L. Vay and G. W. Sachse, *J. Geophys. Res.*, 2004, **109**, DOI: 10.1029/2003JD004362.
58 Y. X. Wang, M. B. McElroy, T. Wang and P. I. Palmer, *J. Geophys. Res.*, 2004, **109**, DOI: 10.1029/2004JD005250.
59 G. L. Hutchinson, M. F. Vigil, J. W. Doran and A. Kessavalou, *Nutr. Cycl. Agroecosyst.*, 1997, **48**, 25.
60 J. Ludwig, F. X. Meixner, B. Vogel and J. Forstner, *Biogeochemistry*, 2001, **52**, 225.
61 E. Sanhueza, *Nutr. Cycl. Agroecosyst.*, 1997, **48**, 61.
62 U. Skiba, D. Fowler and K. A. Smith, *Nutr. Cycl. Agroecosyst.*, 1997, **48**, 139.
63 D. J. Jacob and P. S. Bakwin, in *Microbial Production and Consumption of Greenhouse Gases: Methane, Nitrogen oxides, and Halomethanes*, ed. J. E. Rogers and W. B. Whitman, American Society for Microbiology, Washington DC, 1991, p. 237.
64 L. N. Ganzeveld, J. Lelieveld, F. J. Dentener, M. C. Krol, A. J. Bouwman and G. J. Roelofs, *J. Geophys. Res.*, 2002, **107**, DOI: 10.1029/2001JD001289.
65 C. S. Potter, P. A. Matson, P. M. Vitousek and E. A. Davidson, *J. Geophys. Res.*, 1996, **101**, 1361.
66 E. A. Davidson and W. Kingerlee, *Nutr. Cycl. Agroecosyst.*, 1997, **48**, 37.
67 X. Y. Yan, H. Akimoto and T. Ohara, *Global Change Biol.*, 2003, **9**, 1080.
68 A. F. Bouwman, L. J. M. Boumans and N. H. Batjes, *Global Biogeochem. Cycles*, 2002, **16**, DOI: 10.1029/2001GB001812.
69 FAO, *Current world fertilizer trends and outlook to 2008/09*, Food and Agriculture Organization of the United Nations, Rome, 2004.